Structural, chemical, and magnetic investigation of a graphene/cobalt/platinum multilayer system on silicon carbide

P Weinert[1], J Hochhaus[1], L Kesper[1], R Appel[1], S Hilgers[1],
M Schmitz[1], M Schulte[1], R Hönig[1], F Kronast[2], S Valencia[2],
M Kruskopf[3], A Chatterjee[3], U Berges[1] and C Westphal[1]

[1] Fakultät Physik/DELTA, TU Dortmund University, D-44221 Dortmund, Germany
[2] Helmholtz-Zentrum Berlin für Materialien und Energie, D-12489 Berlin, Germany
[3] Physikalisch-Technische Bundesanstalt (PTB), D-38116 Braunschweig, Germany

E-mail: philipp.weinert@tu-dortmund.de

Abstract

We investigate the magnetic interlayer coupling and domain structure of ultra-thin ferromagnetic (FM) cobalt (Co) layers embedded between a graphene (G) layer and a platinum (Pt) layer on a silicon carbide (SiC) substrate (G/Co/Pt on SiC). Experimentally, a combination of x-ray photoemission electron microscopy with x-ray magnetic circular dichroism has been carried out at the Co L-edge. Furthermore, structural and chemical properties of the system have been investigated using low energy electron diffraction (LEED) and x-ray photoelectron spectroscopy (XPS). *In situ* LEED patterns revealed the crystalline structure of each layer within the system. Moreover, XPS confirmed the presence of quasi-freestanding graphene, the absence of cobalt silicide, and the appearance of two silicon carbide surface components due to Pt intercalation. Thus, the Pt-layer effectively functions as a diffusion barrier. The magnetic structure of the system was unaffected by the substrate's step structure. Furthermore, numerous vortices and anti-vortices were found in all samples, distributed all over the surfaces, indicating Dzyaloshinskii–Moriya interaction. Only regions with a locally increased Co-layer thickness showed no vortices. Moreover, unlike in similar systems, the magnetization was predominantly in-plane, so no perpendicular magnetic anisotropy was found.

Keywords: epitaxial graphene, metal intercalation, x-ray photoemission electron microscopy,
magnetic imaging, Dzyaloshinskii–Moriya interaction, graphene-ferromagnet interface

1. Introduction

The ongoing tremendous development of electronic devices with the aim of further miniaturization while increasing performance leads to several major and further growing challenges, such as a need for reduced power consumption and improved heat dissipation [1]. The field of spintronics [2] offers solutions to these challenges, as it provides enormous potential for high-density data storage, high processing speed, and low power requirements [3–6]. Within this research field, effects such as giant magnetoresistance (GMR) [7–9] and tunnel magnetoresistance (TMR) [10–12] enable a wide variety of applications. For instance, magnetoresistive random access memories (MRAM), MRAMs with spin-transfer torque (STT-MRAM), and magnetic field sensors are the subject of current research [13, 14].

In order to exploit the potential of spintronic applications, there is a need for suitable spin transport channels, topologically stable spin textures, and fast motion of chiral textures [15]. One promising candidate in this context is graphene since it is known for its long spin-lifetime and diffusion-
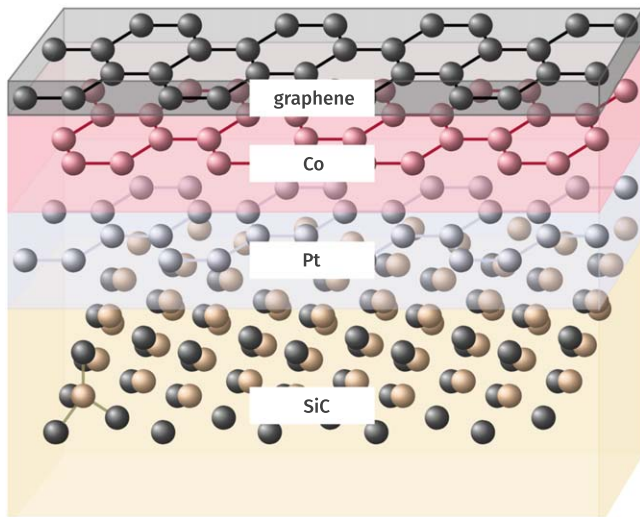
Figure 1. Sketch of the G/Co/Pt sample system on SiC.

length of several micrometers even at room temperature, making it extremely interesting for applications such as in lateral spin-transport devices [16]. Combining graphene with a ferromagnet like Co leads to many advantageous effects, such as Dzyaloshinskii–Moriya interaction (DMI), a strong Rashba effect, and spin filtering [17, 18]. Moreover, it enhances perpendicular magnetic anisotropy (PMA) in Co and other transition metals [15, 19–21], which stabilizes magnetization states over a long time [22–29]. Another method of inducing PMA in Co was recently shown by combining it with a heavy non-magnetic metal such as Pt [30, 31]. A Co/Pt system also offers the possibility of spin-based high-density memory storage as well as high domain-wall velocities due to its chiral Néel-type magnetic domain walls [15]. This feature allows for high processing speed in future applications [32].

In this study, we investigated the combined G/Co/Pt system prepared on silicon carbide (SiC) to unite the respective mentioned beneficial properties of the G/Co and Co/Pt systems. Figure 1 shows a schematic sketch of the system. Next to the magnetic structure, its chemical and general structural properties were studied as a basis for future spintronic applications. In addition to all mentioned advantageous characteristics, the inert properties of graphene protect the sample surface from oxidation [33]. Below the surface, cobalt silicide formation is suppressed by the Pt-layer, serving as a diffusion barrier up to certain temperatures [34]. Cobalt silicides are suspected of weakening the Co-layer's magnetic order [31, 35–37].

DMI and PMA were reported in G/Co/Pt system prepared on MgO(111) [15]. In that study, a rather thick Pt-layer of 300 Å reduced the influence of the substrate. In the present study, we tried to obtain an experimental indication of the substrate's influence. Thus we studied thin films of Pt ranging from 3 to 8 Å. The SiC-substrate offers several decisive advantages. Most importantly, the film quality of graphene grown on SiC is of utmost quality. For instance, in contrast to others, on this substrate, single crystallographic graphene

domains were reported over exceptionally large areas [15, 33]. Further, graphene grown on SiC shows a very high spin injection efficiency [38].

Here, we utilized intercalation to prepare ultra-thin metal layers beneath the $(6\sqrt{3} \times 6\sqrt{3})$ R30°-reconstruction of the SiC. The method is well-established for many different materials, such as H_2 [39], Au [40, 41], and next to Co [31], further 3d-metals like Fe [42] and Cu [43]. A range of distinct properties of the resulting system can be tailored by selecting the metal and specifying its thickness beneath graphene [39, 44, 45].

In the present study, low energy electron diffraction (LEED) and x-ray photoelectron spectroscopy (XPS) were used to analyze the structural and chemical properties of the system. These techniques revealed the crystalline structure of each layer of the system, including a $(4\sqrt{3} \times 4\sqrt{3})$ R30°-reconstruction for the Pt-layer, and proved that the Pt-layer effectively functions as a diffusion barrier, preventing the formation of cobalt silicides. The magnetic domain structure was studied by means of x-ray photoemission electron microscopy (X-PEEM) in combination with x-ray magnetic circular dichroism (XMCD). A predominantly in-plane magnetization with numerous vortices and anti-vortices was found in all samples. The vortices indicate the presence of DMI. They were distributed over the entire sample surfaces and since the magnetization is in-plane, they were found to be merons, anti-merons, and bimerons [46].

2. Methods

2.1. Sample preparation

All samples investigated were cut from on-axis 4H-SiC (n-type) wafers from Cree, NC, USA, which had been chemically-mechanically polished (cmp) and had an epi-ready (0001) surface. Homogeneous large-area and single-domain growth of the $(6\sqrt{3} \times 6\sqrt{3})$ R30° surface reconstruction of SiC, also known as buffer-layer, was achieved by confinement controlled sublimation (CCS) [47].

Before sublimation, all wafers were cleaned and degassed. The cleaning process started with an ultrasonic bath in acetone, followed by isopropanol for 10 min each. Subsequently, a dip in 5% hydrofluoric acid (HF) for 5 min was carried out to remove oxide contamination from the surface [48]. Degassing was carried out in a vacuum with a base pressure below 2×10^{-8} mbar at 700 °C for 3 h. In the next step, Si sublimation was conducted in an inductively heated graphite crucible, in 900 mbar Ar at 1500 °C for 30 min, resulting in the formation of a homogenous $(6\sqrt{3} \times 6\sqrt{3})$ R30° surface reconstruction all over the sample [47]. Only very small graphene monolayer stripes were observed at step-edges in the PEEM images. The height and width of these steps are some nm and several μm, respectively [31, 49]. To investigate the influence of the buffer-layer's flatness on the magnetic domain structure, some samples were prepared by the modified polymer-assisted sublimation growth (PASG) method. This technique allows for the growth

of ultra-smooth graphene and buffer-layers with step-bunching-free ultra-small terrace heights of only one or two SiC layers [50]. This is the most important criterion for good quality buffer- and graphene layer, resulting in enhanced electron mobility and increased charge carrier densities [51]. For samples used in this study, a low miscut wafer ($-0.03°$ towards the primary flat) was used with a polymer solution of volume ratio $AZ(\mu l)/IPA(ml)$ of 3.4 for pre-treatment. Buffer-layer growth was carried out at $1450\,°C$ for 10 min and 1 bar Ar pressures.

Regardless of the buffer layer preparation method, subsequently, the samples were inserted into another vacuum chamber and annealed at $550\,°C$ for 3 h. The base pressure was below 2×10^{-10} mbar.

The sample surface was covered with Pt by physical vapor deposition (PVD) and annealed to initiate intercalation. The same steps were repeated for Co. During metal deposition, all samples were kept at room temperature. The deposition rates were determined using a quartz crystal microbalance to be $t_{Pt} = 0.025$ Å min^{-1} and $t_{Co} = 0.38$ Å min^{-1}. The Pt-film thickness was chosen to be 4 Å. Initial investigations showed that this thickness is sufficient to fully decouple graphene from the substrate. The Co-film thicknesses of 1.5 nm, 2.6 nm, and 3.4 nm were selected. These are thick enough to form a complete layer after intercalation, and for a film thickness of at least 3.0 nm, the magnetic domains cover several terraces [31]. Layers thicker than 4.0 nm are not expected to exhibit strong PMA [15].

2.2. Characterization

In order to determine the temperatures necessary to intercalate Pt and Co, a systematic and comprehensive preparation series was carried out. The prepared surfaces were studied by UV-PEEM. The corresponding images are presented in the appendix information in figures A1 and A2.

Sample heating was performed by direct heating and sample temperature was controlled by an infrared pyrometer (IMPAC IGA 6/23 Advanced, LumaSense). The maximum sample temperature was $900\,°C$.

Samples were characterized by LEED and XPS in all preparation steps. The surface periodicity was checked by LEED, while XPS spectra were recorded to identify contaminations, chemical bonding states, and the order of surface layers. These spectra were recorded at the PGM beamline 11 at the synchrotron radiation source DELTA, Germany.

To investigate the magnetic structure and anisotropy of the embedded Co-layer, X-PEEM in combination with XMCD at the Co L_3-edge was used [52, 53]. All X-PEEM images were acquired with the Elmitec PEEM-III energy microscope at the UE49-PGM beamline at the BESSY II electron storage ring, Berlin, Germany.

The energy and helicity of the incoming photons were tuned to gain chemical and magnetic sensitivity, respectively. By recording XMCD images for azimuthal sample angles at $0°$, $90°$, and $180°$, the 2D magnetic structure can be determined [53]. The incident photon beam impinged the sample at a grazing angle of $16°$.

3. Results

3.1. Structural properties

Figure 2 shows LEED patterns of the sample system in different preparation states. Figure 2(a) shows the pattern of the prepared SiC surface. Next to two series of hexagonally ordered spots originating from the substrate and the graphene, a variety of spots caused by the $(6\sqrt{3} \times 6\sqrt{3})$ R30°-reconstruction are visible. The individual spot-brightnesses within this image are characteristic of different numbers of graphene layers. Here, a small amount of graphene can be identified, which preferably forms as small stripes at the substrate's step edges. These stripes form while the first carbon layer is still spreading over the surface during sublimation, making them unavoidable for the preparation of a complete reconstruction layer [31, 54, 55].

After deposition of only 4 Å Pt, the LEED pattern disappears completely, indicating a homogeneous and non-periodic coverage. Subsequently, the samples were heated to the previously determined annealing temperature in order to initiate the intercalation process (see appendix A.1). For all investigated Pt-film thicknesses, no changes in the LEED patterns were observed below $700\,°C$. After annealing at this temperature, the hexagonally ordered graphene- and SiC-spots reappeared. Simultaneously, the $(6\sqrt{3} \times 6\sqrt{3})$ R30°-reconstruction remained absent, indicating decoupling and partial lifting of the carbon layer. Thus, the buffer-layer became quasi-freestanding graphene. In addition, a $(4\sqrt{3} \times 4\sqrt{3})$ R30°-reconstruction appeared, which is assigned to the intercalated Pt-layer. At a temperature of $T_{Pt} = 720\,°C$ and above, these spots became significantly more pronounced, while no further changes were found up to temperatures of $900\,°C$. A corresponding image is shown in figure 2(b). All samples shown here were annealed at T_{Pt} to induce the intercalation of Pt.

These results are consistent with those reported by Xia *et al* [56]. However, in our study, we find additional spots surrounding each SiC spot, as visible in figure 2(b). These additional spots allowed us to identify the superstructure. This difference can be explained by the increased Pt-layer thickness used in this work. Also, the electron kinetic energy of $E_{kin} = 95$ eV used to record the LEED image corresponds to a slightly larger mean-free path. Within our study, we find an improved spot sharpness and brightness due to the increased layer thickness and increased mean-free path of electrons.

Additionally, acquired UV-PEEM images also confirm that Pt successfully intercalates for annealing temperatures of T_{Pt} or higher, indicated by the reappearance of the initial step-structure of graphene. Furthermore, similar to the results of Xia *et al*, a first change after annealing at $550\,°C$ can be identified. This might be caused by Pt tending to wet the surface [57], preferably at terraces. Corresponding PEEM images and further information are provided in appendix A.1. In the last phase of the preparation, Co deposition leads to the disappearance of the pattern, as already observed during Pt-deposition. Based on the study of Hönig *et al* [31], $T_{Co} = 325\,°C$ was found to be sufficient for Co intercalation with a Co-layer thickness ranging from 1.5 to 3 nm. Figure 2(c) shows the LEED pattern of a sample
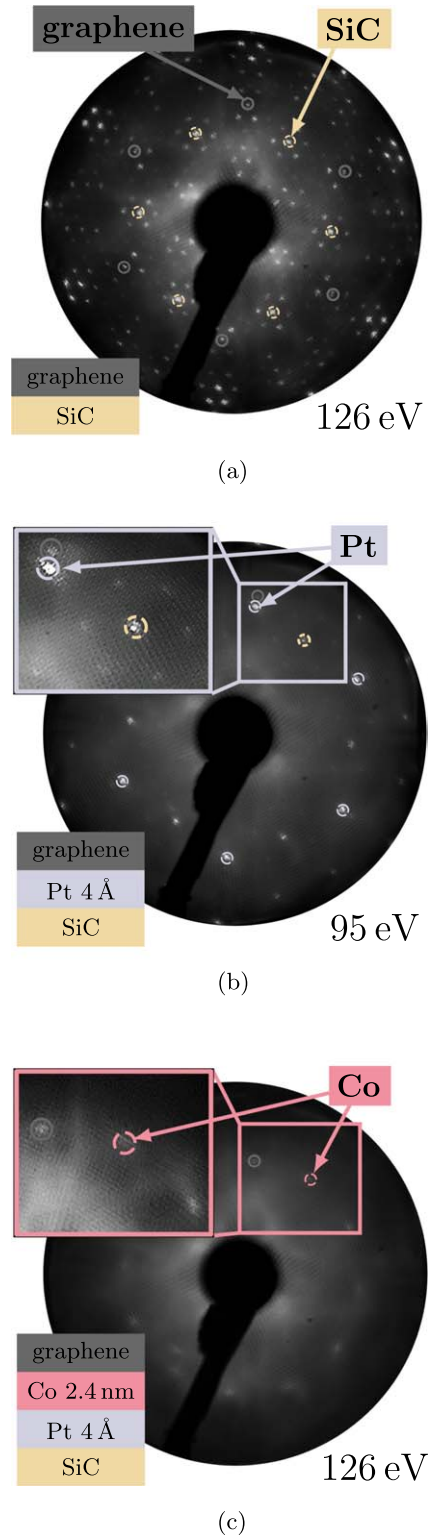
Figure 2. LEED patterns of the sample system various preparation steps. The individual step is depicted in each image. LEED-spots of graphene, SiC, Pt, and Co are indicated in gray, yellow, silver, and red, respectively. (a) LEED pattern of a pristine sample, showing the $(6\sqrt{3} \times 6\sqrt{3})$ R30° -reconstruction on SiC. [33], (b) LEED pattern of the sample system after intercalation of 4Å Pt. A $(4\sqrt{3} \times 4\sqrt{3})$ R30°-reconstruction appears, associated to intercalated Pt, and (c) LEED pattern of the sample system after intercalation of 2.4 nm Co. A (1×1) R30°-reconstruction appears, associated to intercalated Co.

after depositing 2.4 nm Co and subsequent annealing. Two sets of hexagonally ordered spots associated with graphene and Co appeared. The Co-pattern is rotated by 30° with respect to the graphene pattern, and it indicates a lattice constant consistent with the one of Co in hcp-structure [58]. Spots of the Pt-layer and the substrate did not reappear due to the rather thick Co-layer. The reappearance of graphene spots after annealing indicates that Co has successfully been intercalated. Also, this is confirmed by the bright appearance of the graphene spots compared to the cobalt spots.

To avoid Si diffusion through the Pt- and Co-layers and to keep Co in an hcp-lattice structure [58], no higher temperatures were used in this preparation phase. However, this relatively low temperature results in the Co spots not being very sharp. This is likely due to limited long-range order, which would also affect the system's magnetic properties. For all Pt- and Co-layer thicknesses investigated, the same spots were visible in the LEED images. We could not identify any differences.

3.2. Chemical properties

The following presents XPS spectra of a sample intercalated with 4 Å Pt and subsequently 3 nm Co.

The chemical composition of the sample was verified by XPS survey spectra. The spectra were recorded at normal emission, i.e. an emission angle of $\Theta = 0°$ and photon energy of $h\nu = 700$ eV. The upper panel of figure 3 shows a spectrum taken before any metal deposition. Characteristic peaks of the Si 2s, Si 2p, and C 1s orbitals, related plasmon-loss features, and two Auger signals are indicated. After intercalation, signals of the Pt 4d, Pt 4f, and Co 3p orbitals, along with the Pt OOO-Auger signal, emerged, as shown in the lower panel of figure 3.

Next, a detailed analysis of the C 1s, Pt 4f, and Co 3p has been carried out. For this, high-resolution spectra were recorded in each preparation step. The C 1s-, Pt 4f-, and Co 3p-spectra were taken at 450 eV, 240 eV, and 180 eV, respectively. Within the analysis, a Shirley background was removed [59]. Subsequently, the spectra were decomposed into components by applying a peak-fitting procedure using the software LG4X-V2 [60]. The area ratio of an element's component at emission angles of $\Theta = 0°$ and $\Theta = 60°$ compared to the area ratio of the other elements' components can be used to determine the arrangement of the elements within the sample.

Figure 4 shows C 1s core level spectra. On the left side, the graphene/SiC spectra are presented. They consist of four components, which are assigned to SiC, graphene, S1, and S2. Within the peak fit procedure, Voigt- and Gauss-Doniach lineshapes were applied [61, 62]. The components S1 and S2 are assigned to carbon atoms with bonds within the uppermost surface layer and with bonds to the underlying Si atoms, respectively. The presence of a small graphene component results from graphene stripe formation at the step edges, as explained earlier. The last component, SiC, originates from the substrate. [33, 54]

The spectra after intercalation of 4 Å Pt and additional 3 nm Co can be seen in the right column of figure 4. After
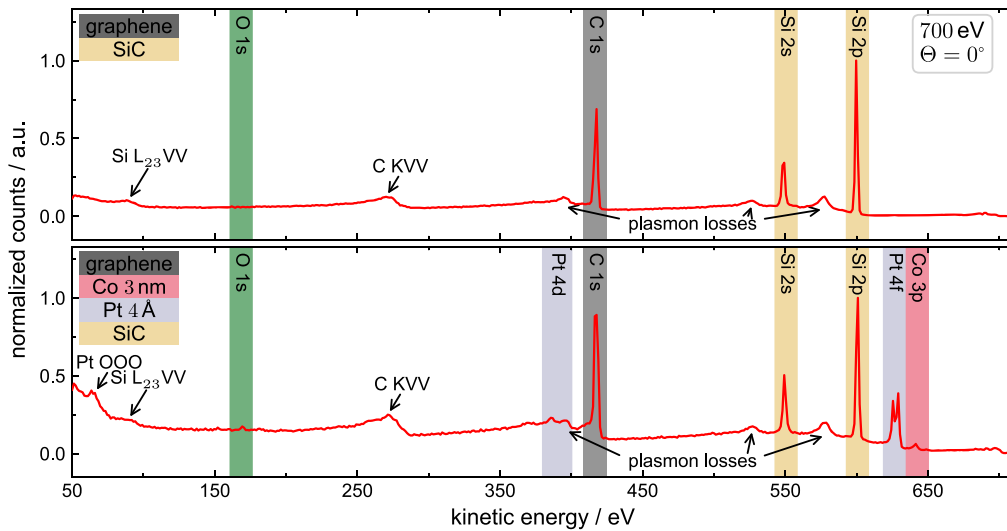
Figure 3. XPS survey spectra of the initial SiC surface reconstruction and after intercalation of 4 Å Pt + 3 nm Co in the upper and lower panel, respectively. The electron signals of the respective elements, plasmon loss features, and Auger signals are assigned in the figure. After intercalation a very weak oxygen contamination was detected, as shown in the green area in the lower panel.
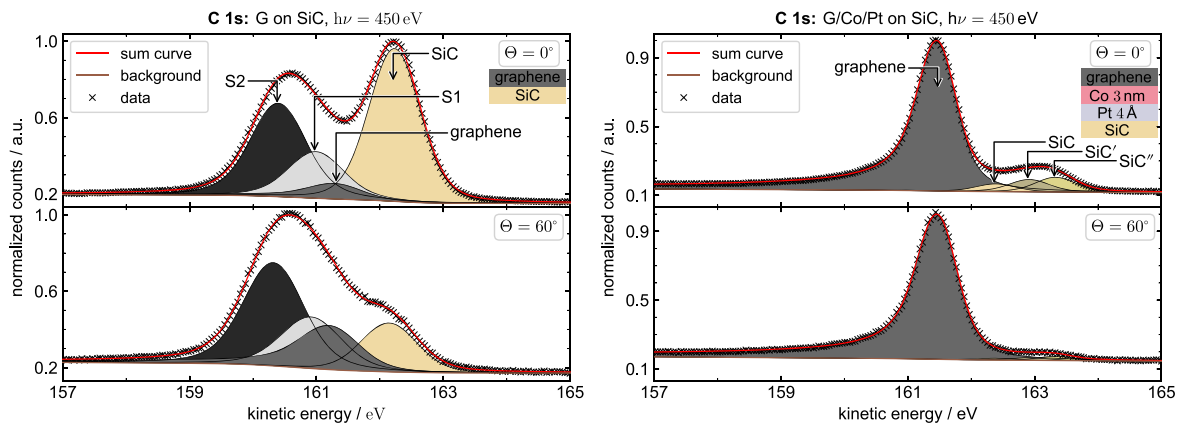

Figure 4. High resolution C 1s XPS spectra of the $(6\sqrt{3} \times 6\sqrt{3})$ R30°-reconstruction on SiC (left) and after intercalating 4 Å Pt + 3 nm Co (right).

intercalation of Pt, photoemission features of the $(6\sqrt{3} \times 6\sqrt{3})$ R30°-reconstruction almost vanished, while the graphene component increased strongly. These findings indicate the decoupling of the carbon layer and its transformation into quasi-freestanding graphene and, thus, a successful intercalation. In addition, two more components, SiC′ and SiC″, appeared, associated with the upper first SiC layers, which are in a changed Coulomb environment now due to the presence of Pt. Comparing the heights of the components in the spectrum taken at $\Theta = 0°$ with those in the spectrum taken at $\Theta = 60°$ supports the assumption that the new components are located at the top of the substrate. Similar effects, with only one additional component, were found for the intercalation of H, Li, and Si [39, 56, 63, 64]. The only effect of Co deposition and intercalation was a slight change in the height ratios of the components.

Next, Co intercalation was verified by angle resolved XPS (ARXPS). Due to annealing, the intensity of the Co signal decreased while the intensity of the C signal increased. This effect is even more pronounced, when

changing the emission angle from normal to grazing emission. A corresponding spectrum can be seen in figure A3 in the appendix.

Figure 5 shows XPS spectra of the Pt 4f doublet. Additionally to the decoupling of the $(6\sqrt{3} \times 6\sqrt{3})$ R30°-reconstruction resulting from the Pt interaction shown in figure 4, we find three peaks from Pt-silicides in the signal, PtSi, Pt_2Si, and Pt_3Si. The left column of figure 5 shows spectra before intercalation. Notably, all three silicides are already present at this preparation phase, but with rather weak photoemission signals. After intercalation, almost all the Pt is bonded to Si, as shown in the spectra in the middle column of figure 5. This clear change indicates that most of the Pt has been intercalated. After the intercalation of cobalt, only the height ratios of the components have changed slightly. Thus, Co intercalation does not alter the chemical structure of the Pt-layer. Corresponding spectra can be seen on the right in figure 5. In all preparation stages, the components in the spectra taken at $\Theta = 0°$ and $\Theta = 60°$ have approximately the same height ratios, which indicates a well-defined and thin Pt-layer.
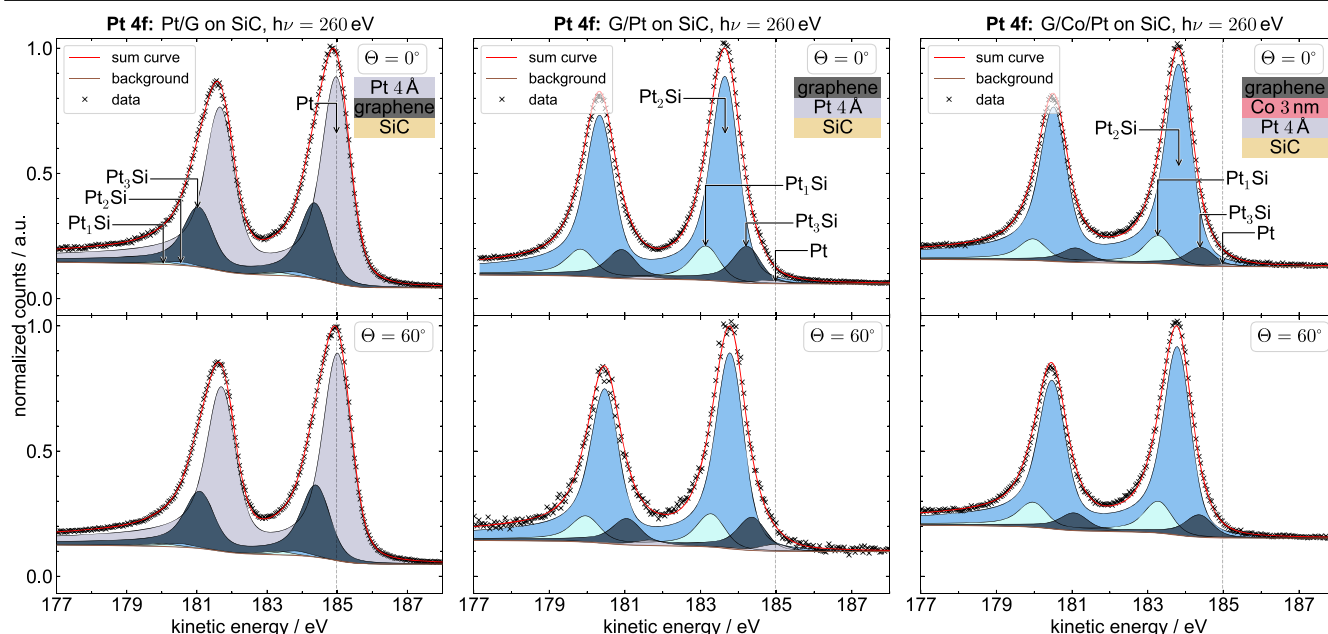
Figure 5. High resolution Pt 4f XPS spectra after deposition of 4 Å Pt (left), after the intercalation of the Pt (middle), and after 4 Å Pt + 3 nm Co intercalation (right).
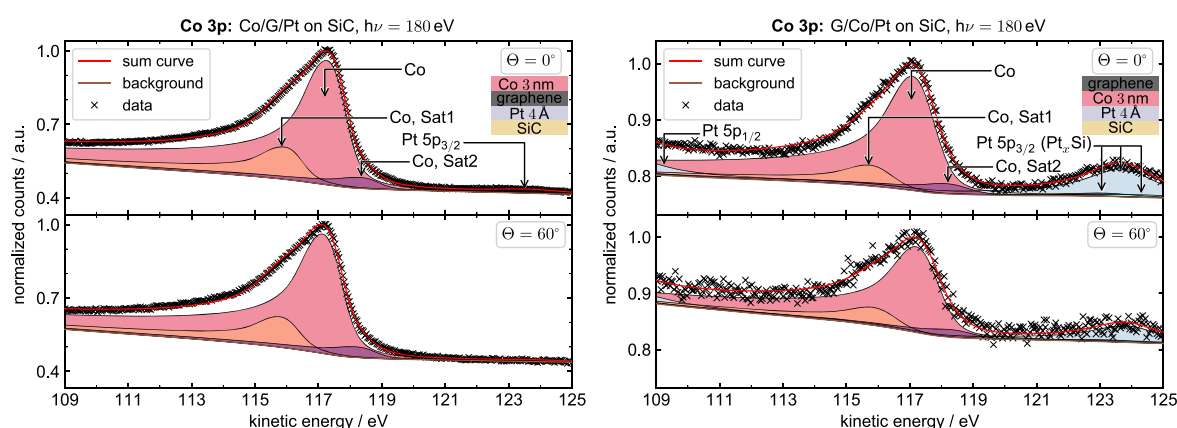

Figure 6. High resolution Co 3p XPS spectra after 3 nm Co-deposition (left) and after the intercalation (right).

The Co 3p spectra before and after intercalation can be fitted with the same components and almost identical height ratios, as displayed in figure 6. This proves the successful prevention of cobalt-silicide formation by intercalating Pt first. Next to the core level signal, two Co-satellite peaks are identified. These are most likely shake-up (Sat1) and shake-down (Sat2) signals [65]. After intercalation, the Co is covered by the carbon layer, resulting in decreased photoelectron intensity. Since the Pt 5p signal is not affected by intercalation, it grew after intercalation compared to the Co 3p signal.

Furthermore, the strong decrease in Co intensity due to the covering by the carbon layer causes the Pt 5p doublet signal to become much more pronounced in comparison after intercalation. However, since the Pt is covered by the Co-layer, its intensity is much larger at $\Theta = 0°$ than at $\Theta = 60°$.

All components present in the spectra shown could also be identified for all other samples of the investigated Pt- and Co-layer thicknesses. Spectra of samples of different

layer thicknesses differ only in the height of individual components.

3.3. Magnetic properties

The magnetization orientation of all Co-layers was investigated after their intercalation was fully completed. To investigate the influence of the preparation on the magnetic properties of the intercalated Co-layer, three different sample sets were prepared. Set **A** was prepared using the CCS-method and treated *ex situ*, set **B** was prepared by the PASG-method and treated *ex situ*, and set **C** was prepared using the CCS method and treated *in situ*. *ex situ/in situ* sample treatment means that the sample was/was not exposed to air between preparation and investigation. All previous investigations were done solely *in situ*. LEED patterns and XPS spectra of samples prepared with the two preparation methods, CCS and PASG, were quasi-identical, we could not

identify a difference. Figure 7 displays X-PEEM images of each sample type.

The first column shows images that depict chemical contrast achieved by x-ray absorption spectroscopy, displaying the morphology of the cobalt films (see appendix A.3). In the second column, images of the in-plane magnetization orientation are presented. These were obtained by combining magnetic contrast XMCD images recorded at the Co L_3-edge at three different azimuthal angles ϕ [52] (For more details, see appendix A.4).

The chemical contrast figures 7(A1) and (B1) are characterized by dark lines indicating the substrate's step edges. Cobalt tends to avoid these edges, due to graphene stripe-formation over the buffer-layer at step edges during preparation. The same was found for Co intercalated graphene on SiC without Pt [31]. However, for sample **A**, Pt intercalation prior to Co resulted in some small regions where no step-edges were visible at all. In figure 7(A1), such a continuously covered region can be observed around the defect in the lower right. Its brighter contrast compared to the rest of the image indicates a locally thicker Co-layer. Continuously covered regions were only found for sample **A**. However, the flatter steps of PASG-samples compared to CCS-samples lead to a weaker contrast between the step edges and the terraces, and many segments of the step edges appear to be covered continuously.

Defects were observed all over the sample surfaces, and examination of several images has shown that samples **A** and **B** exhibited one defect per 220 nm^2, approximately. Since all defects appear dark, they are not caused by Co. Instead, they most likely originate from remaining Pt at the surface, even after most of the Pt had intercalated. A similar observation was reported for Au [66].

Sample **C** was prepared by CCS, followed by intercalation and *in situ* investigation. *in situ* investigation was chosen to avoid any sample modification due to air exposure or subsequent annealing after reinsertion into vacuum. These changes include the diffusion of Co into the substrate, the diffusion of Si to the Co-layer, and possible structural reordering [58]. The corresponding XAS image is presented in figure 7(C1). It differs clearly from figures 7(A1) and 7(B1) in that it exhibits two types of alternating terraces. One type is depicted in homogeneous gray, while the other is displayed in brighter gray with numerous dark dots corresponding to defects. The dot defects most probably indicate dewetted Pt remaining on the surface. This is a common phenomenon caused by the minimization of the surface free energy upon thin film annealing [67]. After further annealing, such dot defects can combine into larger ones, as visible in figures 7(A1) and (B1). The terraces with dot defects are brighter than those without, indicating Co accumulation on them.

Information about the local chemical properties of the different identified regions was gained by XAS intensities spectra. Figure 8 shows the spectra of the continuous region, the terraces, and the step edges of sample **A**. Only the signal-to-noise ratio and the background shape differ between the spectra, indicating no chemical differences of the Co within the different areas. Furthermore, no oxides are visible, and the branching ratio of all areas is in the interval [0.63; 0.67]. For the other samples, the results are comparable.

The in-plane magnetization angles of all samples show a texture-rich structure of different spin vortex formations, indicating a strong DMI. Some close-ups of these formations are presented in figure 9.

Sample **A**: The continuously covered area of figure 7(A1) differs from the rest also by its magnetic structure.

The magnetization direction in this region is much more uniform than that in the stepped ones, as displayed in figure 7(A2). This is probably caused by reduced DMI due to the increased Co-layer thickness [68]. Samples with the other Co-layer thicknesses investigated, i.e. 1.5 nm and 2.6 nm, showed similar results. Only the continuous areas are reduced in size and number in the case of less Co. However, due to time limitations, only images for two azimuthal angles could be acquired during these additional measurements. For that reason, the in-plane angle of these samples had to be calculated using an approximation. Further, in the other sample areas, many vortices are visible, which indicates strong DMI [69]. Exemplary, one is shown in the close-up in figure 9(a). A comparison of the three X-PEEM images taken at different azimuthal angles indicated that the sample is primarily in-plane magnetized. Consequently, the vortices are most probably merons. In fact, all samples are primarily in-plane magnetized, which is in contrast to the studies of similar systems [15, 30]. Since the PtSi bonds are the main difference from other systems, they are most likely the reason why there is no significant PMA present in the studied system.

Sample **B**: Even though the Co-layer in figure 7(B1) seems to be more continuous than in the striped areas in figure 7(A1), the magnetic orientation shown in figure 7(B2) appears similar to the stepped regions in figure 7(A2). For this sample, vortex formations are visible over the entire surface. In figure 9(b), one particularly large one is presented in a close-up.

Sample **C**: The magnetic in-plane angle of the third sample is presented in figure 7(C2). It is particularly striking that the two types of terraces visible in figure 7(C1) are no different in their magnetic structure. Further, the edges between the two types of terraces also do not change the magnetization angle.

The magnetic structure is primarily homogeneous, with many smaller domains of other spin orientations. At the boundaries of these domains to the dominant spin direction, once again, a large number of spin vortices are present. Next to merons, also many bimerons are visible. The potential influence of the numerous defects on the formation of the merons and bimerons was analyzed by comparing their location in the chemical and magnetic contrast images. No correlation was found, indicating no pinning with contribution of the defects. Thus, the formations seem to be solely stable due to topological protection [70]. One bimeron is shown in the close-up in figure 9(c). The centers of the antivortex (left) and the vortex (right) are marked.

Lastly, the orientation of the magnetic domains was compared to the direction of the step edges. Sample **A** shows
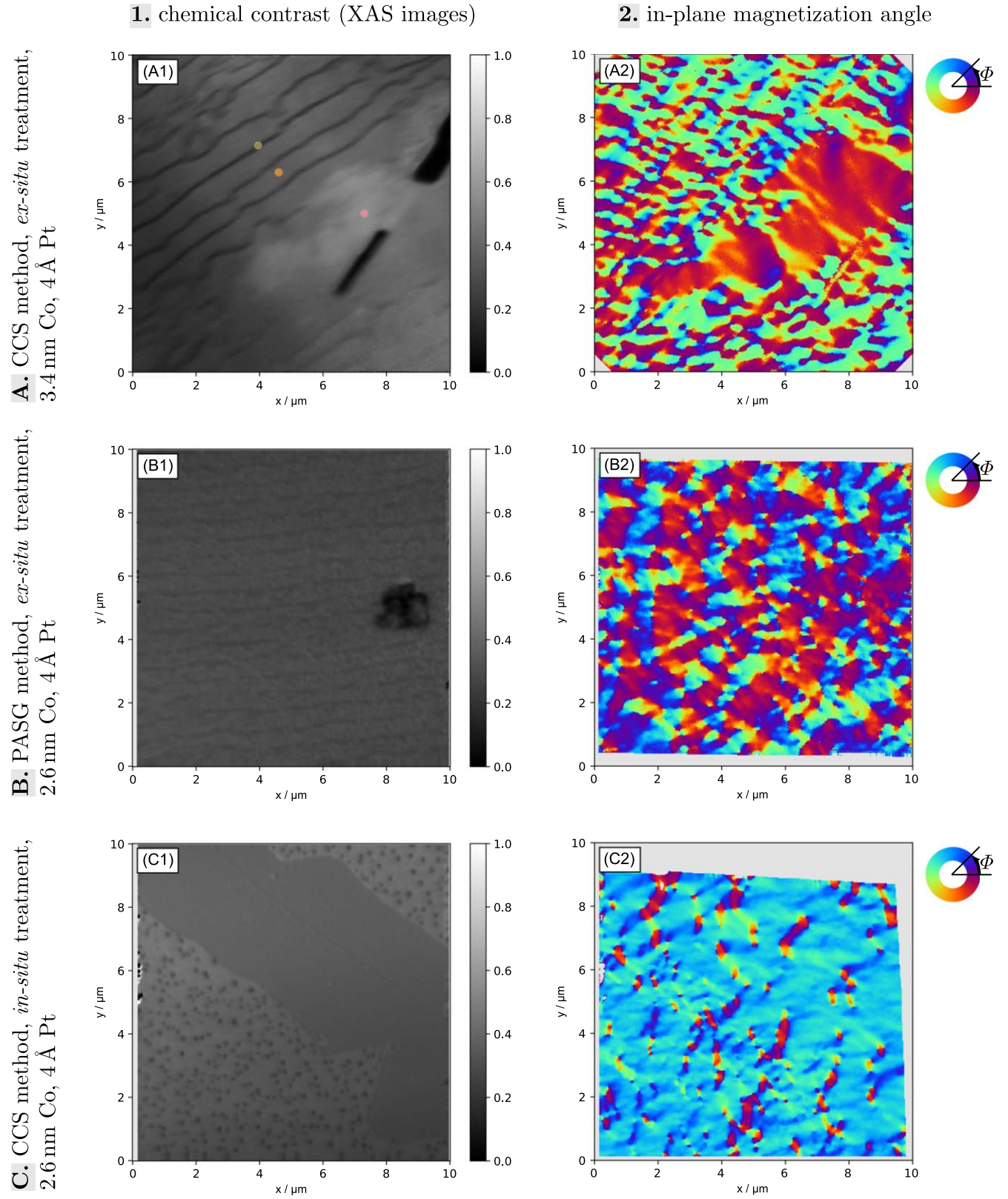
Figure 7. First column: X-PEEM images with chemical contrast (XAS images) recorded at the Co L$_3$-edge. Step edges are visible as dark stripes, indicating that the Co-atoms avoid these areas. In figure 7(A1), three different areas are visible, marked with dots. These are one step edge with a green dot, one terrace with an orange dot, and the continuous area with a red dot. XAS spectra of these areas are shown in figure 8. Second column: in-plane magnetization angle of a Co-layer embedded between graphene and a 4 Å Pt-layer on SiC.
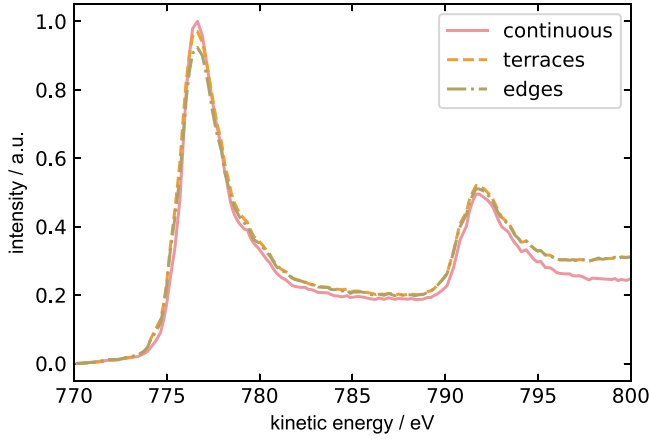
Figure 8. XAS intensities of the three different areas of sample **A** measured around the Co L$_3$-edge. The areas are marked in figure 7(A1).

mainly two types of in-plane domains, which are oriented in opposite directions, and for samples **B** and **C**, one spin direction is predominant in each case. For sample **B**, the direction is almost parallel to the step edges, while no specific alignment was observed for the other samples. However, the alignment of the domains of sample **B** seems to be uncorrelated with the direction of the step edges since the domains reach over them instead of being confined or influenced in any other way. Summarizing the observations, it can be concluded that the step-edge orientation is not correlated with the orientation or shape of the magnetic domains.

4. Conclusion

A graphene/Co/Pt multilayer system on SiC was successfully prepared by intercalating 4 Å Pt on the $(6\sqrt{3} \times 6\sqrt{3})$ R30° reconstructed SiC(0001) surface followed by Co intercalation. The metals form homogeneous films before and after intercalation.

The Pt intercalation lifted the $(6\sqrt{3} \times 6\sqrt{3})$ R30°-reconstruction with the carbon layer becoming quasi-free-standing graphene. Additionally, Pt arranged in a $(4\sqrt{3} \times 4\sqrt{3})$ R30°-reconstruction and PtSi, Pt$_2$Si, as well as Pt$_3$Si are formed due to intercalation. Further, Co-intercalation led to a (1×1)R30°-reconstructed surface. No indication of cobalt-silicide formation was found.

The in-plane magnetization orientation of CCS- and PASG-prepared samples have been investigated by means of X-PEEM in combination with the XMCD. For the samples prepared by CCS and treated *ex situ* (Sample **A**), the step edges are clearly visible in images with chemical contrast. The cobalt's magnetization orientation of these samples is not affected by the step edges. This observation differs from the findings for the system graphene/Co/SiC(0001) without Pt as a diffusion barrier, where magnetic alignment along the step-edges was reported [31]. Furthermore, sample **A** exhibits continuous Co-layers in some regions with a highly ordered
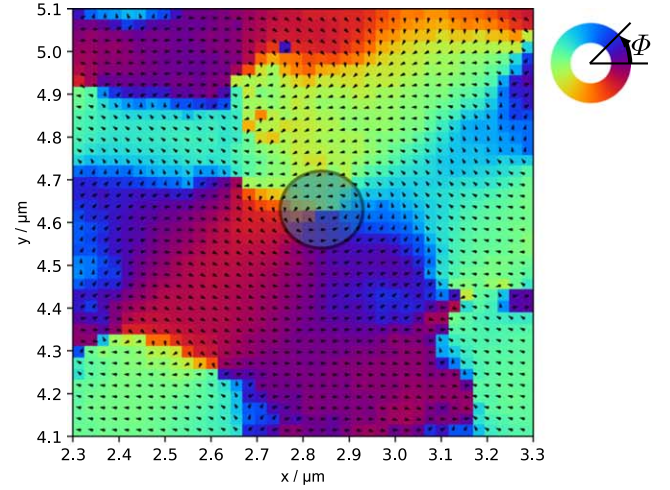
(a) Close-up of sample **A**, showing a meron.
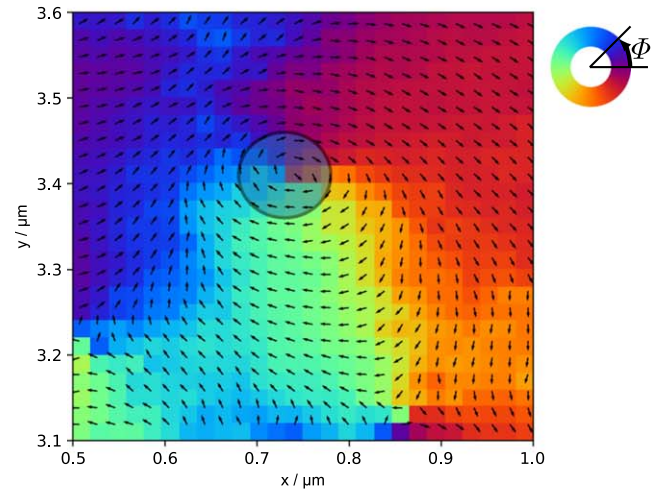
(b) Close-up of sample **B**, showing a meron.
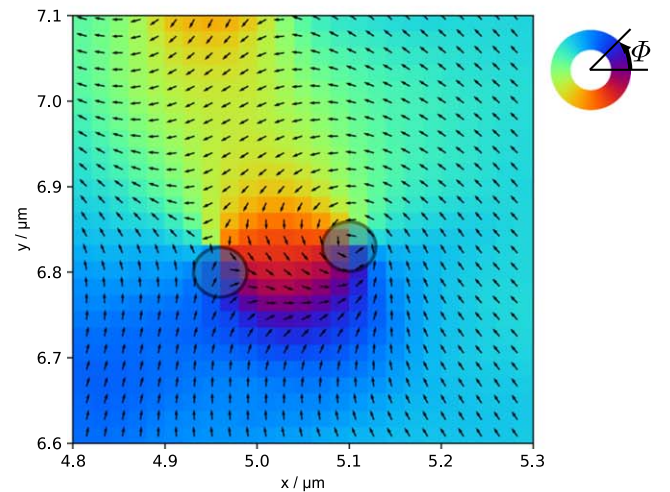
(c) Close-up of sample **C**, showing a bimeron.

Figure 9. Close-ups of different vortex formations of the in-plane magnetization angle of the three types of samples investigated presented in figure 7. Vortex centers are marked. Arrows indicate the spin direction. Values of *x* and *y* are equal to those in the full images.

in-plane magnetization orientation. The brighter XAS contrast in these regions indicate a slightly thicker Co-layer. Samples prepared by the PASG-method showed a stepped structure in their chemical contrast, with many, but only small continuously covered regions. The magnetic orientation of the Co-layer in those samples was highly unordered. In a third step, CCS-method prepared samples with *in situ* treatment were investigated. For this sample type, a primarily homogeneous spin texture appeared together with many smaller domains. Also numerous dot defects were found, which are probably consist of dewetted Pt, which is expected to accumulate to larger defects during additional annealing. Further studies might investigate the influence of the annealing time and temperature on these. All samples reveal numerous merons and bimerons all over the surfaces. Only in the mentioned continuous areas vortices were absent. Potential pinning due to the defects was not observed.

Acknowledgments

Data availability statement

The data cannot be made publicly available upon publication because the cost of preparing, depositing and hosting the data would be prohibitive within the terms of this research project. The data that support the findings of this study are available upon reasonable request from the authors.

Appendix

A.1. UV-PEEM

To find the temperatures for a successful Pt- and Co-intercalation and to check the homogeneity of the deposited metal films, a comprehensive series of preparatory UV-PEEM measurements were performed (exposure time of 4 s), prior to the work analyzing the sample's chemical and magnetic properties. In the PEEM images of the $(6\sqrt{3} \times 6\sqrt{3})$ R30°-reconstruction of SiC, characteristic lines become visible, as shown in figure A1(a). These lines indicate step-edges of the substrate and they result from the unavoidable miscut angle of the substrate. In UV-PEEM images these lines reflect the topographic structure. The $(6\sqrt{3} \times 6\sqrt{3})$ R30°-reconstruction is present on the terraces and is displayed as bright gray stripes. An additional monolayer of graphene accumulates at the step edges. Increasing the preparation time or temperature would cause this monolayer to spread across the terraces, typically indicated by a wavy edge. Furthermore, additional graphene layers would also form. These are characterized by darker contrasts due to their higher work function compared to buffer layer and monolayer graphene [71]. Additional graphene layers could weaken a system's magnetic properties, e.g. the spin lifetime and diffusion coefficient decrease when switching from monolayer to bilayer graphene [16]. However, more studies are needed to make a confident conclusion because other studies are not so clear, e.g. studies on the spin-relaxation mechanism in few-layer graphene are contradictory [72–74]. What can be said is that for multilayer graphene, intercalation would become more difficult since the intercalate would most likely also accumulate between the graphene layers. Furthermore, different SiC-polytypes can lead to different work function contrasts at different terrace regions [75]. After metal deposition, all step edges are covered by an amorphous metal film, rendering the structure invisible in the PEEM images. This observation holds true for all investigated samples, even for the thinnest Pt-layer of 2 Å, which corresponds to an estimated coverage of approximately one monolayer. Thus, a homogeneous coverage is assumed.

After full intercalation, Pt or Co is found below the carbon layer and the step-structure is restored. The temperature initiating intercalation was determined by running preparation cycles consisting of a 5 min annealing step and the recording of a PEEM image. Subsequent preparation cycles started with a 10 °C increased annealing temperature compared to the previous cycle. A series of corresponding images is presented in figure A1. The images have been recorded with a STAIB 350-20 PEEM at TU Dortmund, in combination with a mercury short arc lamp (cut-off energy $h\nu = 4.9$ eV).
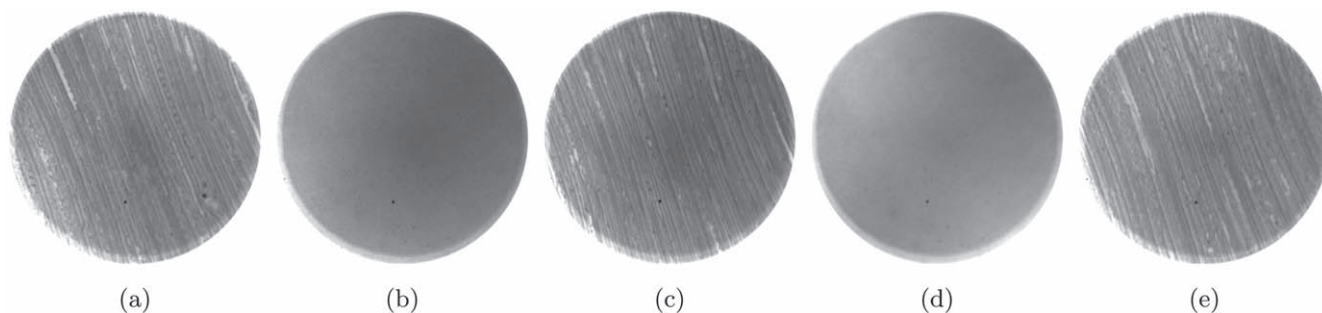

Figure A1. From left to right: UV-PEEM images of the as-prepared $(6\sqrt{3} \times 6\sqrt{3})$ R30°-reconstruction (a), after 4 Å Pt coverage (b), after annealing at 720 °C (c), after 2.6 nm Co coverage (d), and after annealing at 325 °C (e) (FOV 220 μm).
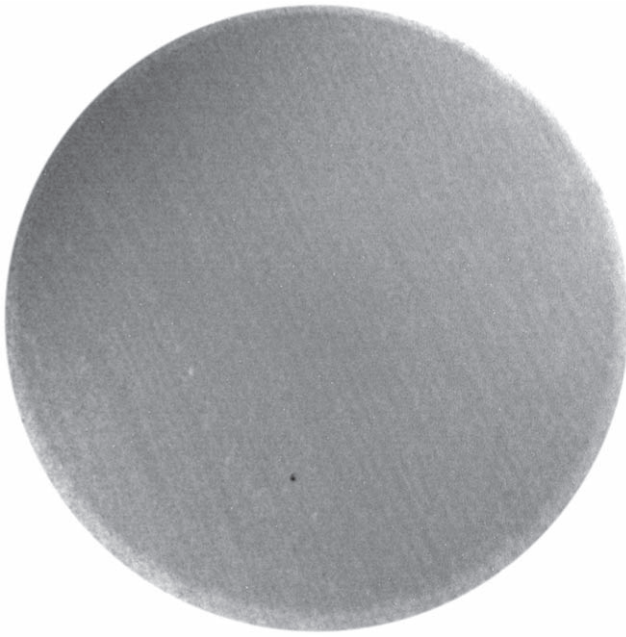
Figure A2. UV-PEEM image of a sample after 4 Å Pt deposition and subsequent annealing at 550 °C (FOV 220 μm).

During the Pt-preparation cycle, the first noticeable change in the PEEM image occurred at 550 °C. After annealing at this temperature, the step structure becomes visible again. However, the steps appear quite blurred, as shown in figure A2. This indicates a structural change in the amorphous Pt-layer. Most likely, it becomes flatter by wetting on the surface, preferably at terraces [57] or also by melting at the surface [76]. As a result, the topography of the Pt-layer becomes more similar to that of the stepped substrate while still being on top of the buffer-layer. Further investigations are required to describe this process precisely. The next change occurred after annealing at 700 °C, which is shown in figure A1(c). After this annealing step, the surface looks like the initial bare buffer-layer. These results are consistent with those of Xia *et al* [56]. After annealing at 900 °C, the highest temperature applied in this study, no further structural or chemical changes were observed in the sample.

Regarding the Co-preparation cycles, an annealing temperature of 325 °C was determined to initiate intercalation, which aligns excellently with the findings of Hönig *et al* [31]. To avoid structural changes from a Co-diffusion into the substrate or from a reorientation of Co-atoms [58] no annealing temperatures above 325 °C were applied.

A.2. ARXPS

After Co deposition and subsequent annealing, no chemical changes were observed. To confirm the successful Co-intercalation, angle resolved x-ray photoelectron spectroscopy (ARXPS) was applied before and after annealing. Here, we compared the ratios of the normalized Co 3p and C 1s photoelectron signals before and after full intercalation as a function of polar angle. In figure A3 the resulting data are presented. The Co 3p signal ratio decreases, while the C 1s
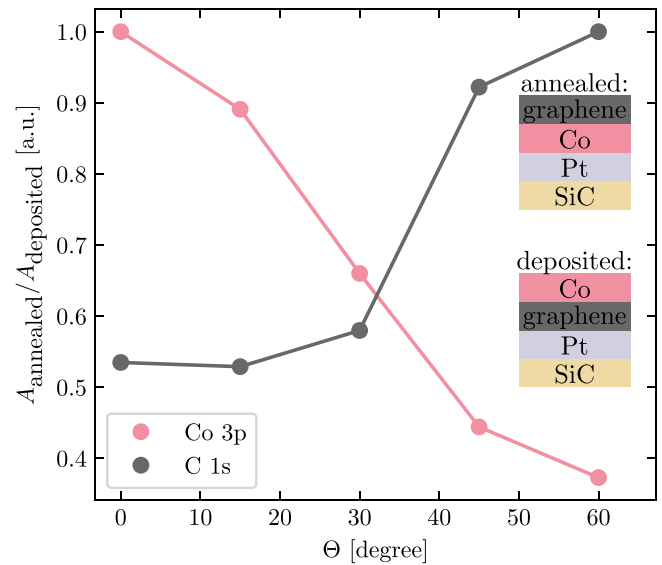

Figure A3. Intensity ratios of normalized XPS intensities after to before annealing of the Co 3p and C 1s signals as a function of polar angle. The Co-layer thickness was 1 nm.

signal ratio increases at high polar angles. This indicates Co intercalated below the top carbon layer due to annealing.

A.3. XAS

In x-ray absorption spectroscopy (XAS), photons excite electrons from core levels to empty states near the Fermi energy. The generated core level holes are filled by other electrons, accompanied by the emission of an Auger electron. Secondary electrons are generated by inelastic scattering processes of Auger electrons. Images with chemical contrast, as in figure 7, present the intensity I given by:

$$I = \frac{I_{\text{edge}} - I_{\text{pre}}}{I_{\text{pre}}}, \tag{A.1}$$

with I_{edge} being the intensity of XAS images taken at the Co L_3-edge and those taken a few eV below I_{pre}. The intensities were measured with both left and right circularly polarized light and were added up. The resulting images provide information about the morphology of the cobalt films, i.e. bright areas indicate much Co while dark areas indicate few Co.

A.4. XMCD

In the following, the dependence of X-PEEM image intensity on the sample surface's magnetization is explained. The analysis used in section 3.3 was carried out according to these explanations.

The geometry of the X-PEEM experiment is shown in figure A4. The sample surface represents the xy-plane. The direction of movement of the photons, given by $\boldsymbol{p}$, is fixed and lies in the xz-plane. It is the same for both light with positive and negative helicity. As mentioned in section 2.2, the angle between the sample surface and the incident photon beam is $16° = 90° - \alpha$. The in-plane and out-of-plane components of
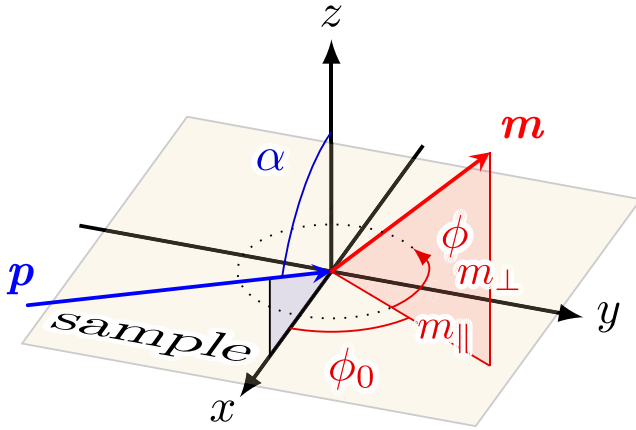
Figure A4. Geometry of the experimental setup. Note that p is shifted in its position compared to equation (A.2) for better visibility. However, only its orientation is relevant to the analysis.

the local surface magnetization m are represented by $m_\parallel$ and $m_\perp$, respectively. The initial azimuthal angle between m and p is given by ϕ_0. For the measurements, the sample was rotated around its normal by ϕ. Therefore, the resulting azimuthal angle of the magnetization direction is given by $\phi_0 + \phi$.

The vectors m and p are connected to the XMCD intensity, which will be used in the following. According to the representation, they are given by:

$$m = \begin{pmatrix} m_\parallel \cos(\phi + \phi_0) \\ m_\parallel \sin(\phi + \phi_0) \\ m_\perp \end{pmatrix}, \quad p = \begin{pmatrix} -\sin(\alpha) \\ 0 \\ -\cos(\alpha) \end{pmatrix}. \quad (A.2)$$

Raw X-PEEM images were recorded with circularly polarized light with both positive and negative helicity at the Co L_3-edge. Exposure time was 3 s. The setup used had a probing depth of a few nm and a lateral resolution of 30 nm [77].

For each surface location and helicity, 40 images were summed to improve statistics. By combining the sums I^x, with x indicating the helicity of the irradiating light, XMCD images are obtained by:

$$I_{\text{XMCD}} = \frac{I^{\text{neg}} - I^{\text{pos}}}{I^{\text{neg}} + I^{\text{pos}}}. \quad (A.3)$$

Division by $I^{\text{neg}} + I^{\text{pos}}$ normalizes the data. This eliminates the effect of a potential uneven irradiation. The intensity I_{XMCD} is proportional to the strength of the surface magnetization $|m|$ and to the cosine of the angle between m and p, given by $\Theta = \angle(m, p)$ [52, 53]:

$$I_{\text{XMCD}} \propto |m| \cos\Theta. \quad (A.4)$$

The right expression in equation (A.4) can also be written as:

$$|m| \cos\Theta = |m| \frac{m \cdot p}{|m| \cdot |p|} \quad (A.5)$$

$$= -m_\parallel \cos(\phi + \phi_0)\sin(\alpha) - m_\perp \cos(\alpha). \quad (A.6)$$

Defining the proportionality constant in equation (A.4) as $-k/\sin(\alpha)$ and introducing $\widetilde{m}_\parallel := km_\parallel$ and $\widetilde{m}_\perp := km_\perp$ finally results in:

$$I_{\text{XMCD}} = \widetilde{m}_\parallel \cos(\phi + \phi_0) + \widetilde{m}_\perp / \tan(\alpha). \quad (A.7)$$

Combining images recorded at three equidistant angles ϕ, here $0°$, $90°$, and $180°$, leads to an analytically solvable system of equations for $\widetilde{m}_\parallel$, ϕ_0, and $\widetilde{m}_\perp$. To solve this system, multiple different cases have to be considered. As a result, $\widetilde{m}_\parallel$, ϕ_0, and $\widetilde{m}_\perp$ can be determined for each pixel of the field of view. The resulting images can be analyzed, e.g., for the relative strength of the in- and out-of-plane components and for structures.

Prior to this calculation, the data was prepared for the analysis. In a first step, image defects and an offset planer were removed without changing the mean intensity. Then, the images of each ϕ-series were rotated and corrected for shift, stretch, and skew so that each surface feature is represented by the same pixels in all images.

ORCID iDs

P Weinert ⓘ https://orcid.org/0009-0008-5586-3686
J Hochhaus ⓘ https://orcid.org/0000-0002-8328-607X
L Kesper ⓘ https://orcid.org/0000-0001-7079-7500
R Appel ⓘ https://orcid.org/0009-0008-6658-9213
S Hilgers ⓘ https://orcid.org/0009-0004-0190-9950
M Schmitz ⓘ https://orcid.org/0000-0001-9060-1122
M Schulte ⓘ https://orcid.org/0000-0002-3409-3490
R Hönig ⓘ https://orcid.org/0000-0001-9259-5862
F Kronast ⓘ https://orcid.org/0000-0001-6048-480X
S Valencia ⓘ https://orcid.org/0000-0002-3912-5797
M Kruskopf ⓘ https://orcid.org/0000-0003-2846-3157
A Chatterjee ⓘ https://orcid.org/0000-0002-7651-4206
U Berges ⓘ https://orcid.org/0000-0002-6934-6486

References

[1] Kish L B 2002 *Phys. Lett.*A **305** 144–9
[2] Wolf S A, Awschalom D D, Buhrman R A, Daughton J M, von Molnár S, Roukes M L, Chtchelkanova A Y and Treger D M 2001 *Science* **294** 1488–95
[3] Hirohata A and Takanashi K 2014 *J. Phys. D Appl. Phys.* **47** 193001
[4] Ahn E C 2020 *npj 2D Mater. Appl.* **4** 17
[5] Makarov A, Windbacher T, Sverdlov V and Selberherr S 2016 *Semicond. Sci. Tech.* **31** 113006
[6] Rajput P J, Bhandari S U and Wadhwa G 2022 *Silicon* **14** 9195–210
[7] Baibich M N, Broto J M, Fert A, Van Dau F N, Petroff F, Etienne P, Creuzet G, Friederich A and Chazelas J 1988 *Phys. Rev. Lett.* **61** 2472–5
[8] Binasch G, Grünberg P, Saurenbach F and Zinn W 1989 *Phys. Rev.*B **39** 4828–30
[9] Parkin S, Li Z and Smith D J 1991 *Appl. Phys. Lett.* **58** 2710–2
[10] Julliere M 1975 *Phys. Lett.*A **54** 225–6
[11] Meservey R and Tedrow P 1994 *Phys. Rep.* **238** 173–243
[12] Moodera J S, Kinder L R, Wong T M and Meservey R 1995 *Phys. Rev. Lett.* **74** 3273

[13] Apalkov D, Dieny B and Slaughter J M 2016 *Proc. IEEE* 104 (IEEE) 1796–830

[14] Freitas P P, Ferreira R and Cardoso S 2016 *Proc. IEEE* 104 (IEEE) 1894–918

[15] Ajejas F *et al* 2018 *Nano Lett.* **18** 5364–72

[16] Han W, Kawakami R K, Gmitra M and Fabian J 2014 *Nat. Nanotechnol.* **9** 794–807

[17] Yang H *et al* 2018 *Nat. Mater.* **17** 605–9

[18] Cobas E D, van't Erve O M J, Cheng S-F, Culbertson J C, Jernigan G G, Bussman K and Jonker B T 2016 *ACS nano* **10** 10357–65

[19] Decker R, Brede J, Atodiresei N, Caciuc V, Blügel S and Wiesendanger R 2013 *Phys. Rev.*B **87** 041403

[20] Vu A-D, Coraux J, Chen G, NDiaye A T, Schmid A K and Rougemaille N 2016 *Sci. Rep.* **6** 24783

[21] Yang H, Vu A D, Hallal A, Rougemaille N, Coraux J, Chen G, Schmid A K and Chshiev M 2016 *Nano Lett.* **16** 145–51

[22] Fukami S, Anekawa T, Zhang C and Ohno H 2016 *Nat. Nanotechnol.* **11** 621–5

[23] Moser A, Takano K, Margulies D T, Albrecht M, Sonobe Y, Ikeda Y, Sun S and Fullerton E E 2002 *J. Phys. D Appl. Phys.* **35** R157

[24] Miron I M, Garello K, Gaudin G, Zermatten P-J, Costache M V, Auffret S, Bandiera S, Rodmacq B, Schuhl S and Gambardella P 2011 *Nature* **476** 189–93

[25] Barlia P, Joshi V K and Bhat S 2021 *J. Comput. Electron.* **20** 805–37

[26] Hanyu T, Endoh T, Suzuki D, Koike H, Ma Y, Onizawa N, Natsui M, Ikeda S and Ohno H 2016 *Proc. IEEE* **104** 1844–63

[27] Quindeau A *et al* 2017 *Adv. Electron. Mater.* **3** 1600376

[28] Naganuma H *et al* 2020 *Appl. Phys. Lett.* **116** 173101

[29] Garcia F, Casali G, Auffret S, Rodmacq B and Dieny B 2002 *J. Appl. Phys.* **91** 6905–7

[30] Nakajima N, Koide T, Shidara T, Miyauchi H, Fukutani H, Fujimori A, Iio K, Katayama T, Ny`vlt M and Suzuki Y 1998 *Phys. Rev. Lett.* **81** 5229–32

[31] Hönig R, Roese P, Shamout K, Ohkochi T, Berges U and Westphal C 2018 *Nanotechnology* **30** 025702

[32] Ajejas F *et al* 2019 *ACS Appl. Mater. Interfaces* **12** 4088–96

[33] Riedl C 2010 Epitaxial graphene on silicon carbide surfaces: growth, characterization, doping and hydrogen intercalation *PhD Thesis* Friedrich-Alexander-Universität Erlangen-Nürnberg

[34] Henry M D and Ahlers C R 2013 *IEEE T. Comp. Pack. Man.* **3** 899–903

[35] Madar R, d'Anterroches C, Arnaud d'Avitaya F, Boursier D, Thomas O and Senateur J P 1988 *J. Appl. Phys.* **64** 3014–7

[36] Ishida K, Nishizawa T and Schlesinger M E 1991 *J. Phase Equilib.* **12** 578–86

[37] Zhou G F and Bakker H 1994 *J. Phys.: Condens. Matter*J. *Phys.: Condens. Matter* **6** 4043

[38] Dlubak B *et al* 2012 *Nat. Phys.* **8** 557–61

[39] Riedl C, Coletti C, Iwasaki T, Zakharov A A and Starke U 2009 *Phys. Rev. Lett.* **103** 246804

[40] Varykhalov A, Sánchez-Barriga J, Shikin A M, Biswas C, Vescovo E, Rybkin A, Marchenko D and Rader O 2008 *Phys. Rev. Lett.* **101** 157601

[41] Premlal B, Cranney M, Vonau F, Aubel D, Casterman D, De Souza M M and Simon L 2009 *Appl. Phys. Lett.* **94** 263115

[42] Shen K, Sun H, Hu J, Hu J, Liang Z, Li H, Zhu Z, Huang Y, Kong L and Wang Y 2018 *J. Phys. Chem.*C **122** 21484–92

[43] Yagyu K, Tajiri T, Kohno A, Takahashi K, Tochihara H, Tomokage H and Suzuki T 2014 *Appl. Phys. Lett.* **104** 053115

[44] Emtsev K V, Zakharov A A, Coletti C, Forti S and Starke U 2011 *Phys. Rev.*B **84** 125423

[45] Toyama H, Akiyama R, Ichinokura S, Hashizume M, Iimori T, Endo Y, Hobara R, Matsui T, Horii K and Sato S 2022 *ACS Nano* **16** 3582–92

[46] Göbel B, Mertig I and Tretiakov O A 2021 *Phys. Rep.* **895** 1–28

[47] De Heer W A, Berger C, Ruan M, Sprinkle M, Li X, Hu Y, Zhang B, Hankinson J and Conrad E 2011 *Proc. Natl Acad. Sci. USA* **108** 16900–5

[48] Dhar S, Seitz O, Halls M D, Choi S, Chabal Y J and Feldman L C 2009 *Am. Chem. Soc.* **131** 16808–13

[49] Kromer H 2016 Epitaktisches Wachstum von graphen mittels der CCS-Methode *MSc Thesis* TU Dortmund University

[50] Chatterjee A, Kruskopf M, Wundrack S, Hinze P, Pierz K, Stosch R and Scherer H 2022 *ACS Appl. Electronic Mater.s* **4** 5317–25

[51] Kruskopf M, Pakdehi D M, Pierz K, Wundrack S, Stosch R, Dziomba T, Götz M, Baringhaus J, Aprojanz J and Tegenkamp C 2016 *2D Mater.* **3** 041002

[52] Stöhr J and Siegmann H C 2006 *Magnetism* ed M Cardona (Springer) 5th edn vol 5, pp 389–97

[53] Kuch W, Schäfer R, Fischer P and Hillebrecht F U 2014 *Magnetic Microscopy of Layered Structures* ed G Ertl and H Lüth (Springer) vol 57, pp 86–96

[54] Riedl C, Coletti C and Starke U 2010 *J. Phys. D: Appl. Phys.* **43** 374009

[55] Emtsev K V, Bostwick A, Horn K, Jobst J, Kellogg G L, Ley L, McChesney J L, Ohta T, Reshanov S A and Röhrl J 2009 *Nat. Mat.* **8** 203–7

[56] Xia C, Johansson L I, Niu Y, Zakharov A A, Janzén E and Virojanadara C 2014 *Carbon* **79** 631–5

[57] Yu R, Song H, Zhang X-F and Yang P 2005 *J. Phys. Chem.*B **109** 6940–3

[58] Nishizawa T and Ishida K 1983 *Bull. Alloy Phase Diagr.* **4** 387–90

[59] Shirley D A 1972 *Phys. Rev.*B **5** 4709

[60] Hochhaus J A and Hideki N 2023 *LG4X-V2 (V2.1.2)* (Zenodo) (https://doi.org/10.5281/zenodo.7777422)

[61] Armstrong B H 1967 *J. Quant. Spectrosc. Radiat. Transfer* **7** 61–88

[62] Doniach S and Sunjic M 1970 *J. Phys. C: Solid State Phys.* **3** 285

[63] Virojanadara C, Watcharinyanon S, Zakharov A A and Johansson L I 2010 *Phys. Rev.*B **82** 205402

[64] Xia C, Watcharinyanon S, Zakharov A A, Yakimova R, Hultman L, Johansson L I and Virojanadara C 2012 *Phys. Rev.*B **85** 045418

[65] Bagus P S, Ilton E S and Nelin C J 2013 *Surf. Sci. Rep.* **68** 273–304

[66] Gierz I, Suzuki T, Weitz R T, Lee D S, Krauss B, Riedl C, Starke U, Höchst H, Smet J H and Ast C R 2010 *Phys. Rev.* B **81** 235408

[67] Thompson C V 2012 *Annu. Rev. Mater. Res.* **42** 399–434

[68] Cho J *et al* 2015 *Nat. Commun.* **6** 7635

[69] Wei W-S, He Z-D, Qu Z and Du H-F 2021 *Rare Met.* **40** 3076–90

[70] Braun H-B 2012 *Adv. Phys.* **61** 1–116

[71] Mammadov S, Ristein J, Krone R, Raidel C, Wanke M, Wiesmann V, Speck F and Seyller T 2017 *2D Mater.* **4** 015043

[72] Yang T-Y *et al* 2011 *Phys. Rev. Lett.* **107** 047206

[73] Han W and Kawakami R K 2011 *Phys. Rev. Lett.* **107** 047207

[74] Sarma S D, Adam S, Hwang E H and Rossi E 2011 *Mod. Phys. Rev.* **83** 407

[75] Wiets M, Weinelt M and Fauster T 2003 *Phys. Rev.*B **68** 125321

[76] Wang Z L, Petroski J M, Green T C and El-Sayed M A J 1998 *J. Phys. Chem.* B **102** 6145–51

[77] Kronast F, Schlichting J, Radu F, Mishra S K, Noll T and Dürr H A 2010 *Surf. Interface Anal.* **42** 1532–6